Appl Nanosci (2017) 7:731–745
https://doi.org/10.1007/s13204-017-0616-5

ORIGINAL ARTICLE

Effect of alkali earth oxides on hydroxy-carbonated apatite nano layer formation for SiO_2–BaO–CaO–Na_2O–P_2O_5 glass system

P. Kiran[1] · V. Ramakrishna[2] · H. D. Shashikala[1] · N. K. Udayashankar[1]

Received: 16 June 2017 / Accepted: 4 October 2017 / Published online: 13 October 2017

Abstract Barium soda lime phosphosilicate [(58SiO_2–(32 − x)BaO–xCao–6Na_2O–4P_2O_5 (where x = 15, 20, 25 and 30 mol%)] samples were synthesised using conventional sol–gel method at 700 °C sintering temperature. Thermal, structural properties were studied using thermo gravimetric analysis and differential thermal analysis, X-ray diffraction, scanning electron microscopy, fourier transform infrared and Raman spectroscopy. Using Raman spectra non-bridging oxygen concentrations were estimated. The hydroxy-carbonated apatite (HCA) layer formation on samples was analysed for 7 days using simulated body fluid (SBF) soaked samples. The growth of HCA layers self-assembled on the sample surface was discussed as a function of NBO/BO ratio. Results indicated that the number of Ca^{2+} ions released into SBF solution in dissolution process and weight loss of SB-treated samples vary with NBO/BO ratio. The changes in NBO/BO ratios were observed to be proportional to HCA forming ability of barium soda lime phosphosilicate glasses.

Keywords Sol–gel · SBF solution · NBO/BO · HCA

Introduction

Bioactive glass and glass-ceramics are well-known reactive materials and can be integrated into human body where they can form biologically active apatite (Hydroxy apatite) layer at the bone/implant interface. Due to this reason they act as the fillers for bioactive composites (Bramhill et al. 2017; Greenspan et al. 1994, 1997, 1998). It is important to note that the bond between a glass material and the bone is a precipitation of an apatite layer on the surface of the glass material which is responsible for bioactivity. The mechanism for bone bonding is attributed to a hydroxy-carbonated apatite (HCA) layer on the glass surface, based on initial glass dissolution (Hench et al. 1971). Hydroxy carbonated apatite is similar to bone mineral and it interacts with collagen fibrils to integrate with the host bone (Hench and Polak 2002). For tissue engineering applications, it is essential that the nucleation and growth of hydroxy apatite (HA) layer be fast on the surface of the bioglass surface in a precise reaction time in body environment (Kokubo et al. 1990; Sooksaen et al 2015; Yousef et al. 2014).

The HA growth rate is strongly influenced by the glass synthesis processes such as sol–gel processes, melt quenching technique, etc. (Catauro et al. 2016). Sol–gel glasses can be produced at low temperature conditions with good homogeneity. The sol–gel method offers potential benefits for obtaining the powdered materials with good control of composition, microstructure, and wider range of bioactivity (Ahmed et al. 2012; Bellucci et al. 2012; Goller et al. 2004; Arcos and Vallet-Regíl 2010). Sol–gel process is a more convenient technique than melt quenching technique to improve HCA layer growth rate in simulated body fluid (SBF) solution based on dissolution property of synthesised glass–ceramics in SBF solution. SBF is a solution ionic concentration close to that of human blood

✉ P. Kiran
sr.kirankumarsr@gmail.com

[1] Department of Physics, Crystal Growth Laboratory, National Institute of Technology Karnataka, Surathkal 575025, India

[2] Hamburg Center for Ultrafast Imaging (CUI), University of Hamburg, Luruper Chaussee 149, 22761 Hamburg, Germany

plasma (Kokubo and Takadama 2006). Energy dispersive X-ray (EDS or EDX) analysis is an important characterisation technique for the identification of presented elements in the sample. Using EDX analysis it can be confirmed whether formed layer in dissolution process is HCA or not, by the identification of Ca, P, O and C elements (Goldstein 2003). Based on higher rate of dissolution in SBF solution these glass samples have implications for biomedical applications such as tissue engineering, bone bonding ability, cancer therapy, etc. (Hashmi et al. 2014; Peitl et al. 2001; Lukito et al. 2005; Sooraj Hussain et al. 2004; Laczka et al. 1999).

CaO/P_2O_5 ratio actually influences the HCA growth rate in SBF solution for calcium phospho silicate glasses (Sopcak et al. 2015; Rogar et al. 2017; Fateme and Saeed 2013). Network modifiers can break the glass structure leading to non-bridging oxygen [NBO] formation. The formation of non-bridging oxigen results in the softening of the glass-ceramic structure. In particular, the NBO/BO ratios affect its bio activity (Lucia et al. 2009). Raman spectroscopy is a powerful tool for non bridging oxygen identification and for finding the concentration of non bridging oxygens in glass matrix (Gonz_alez et al. 2003). Based on the sintering temperature, bio-activity of sol–gel SiO_2–CaO–P_2O_5 bio glass can influence the wollastonite or psudo-wollastanite structure formation after SBF treatment (Ma et al. 2010). Li_2O addition to the calcium phosphosilicate glass resists the HCA growth rate in dissolution process; the problem of HCA layer growth rate resistance in SBF-soaked calcium phosphosilicate glasses can be overcome by Na_2O addition (Kavitha et al. 2014; Lusvardi et al. 2009). Catauro et al. (2016) reported that melt quenched 47S SiO_2–CaO–P_2O_5–Na_2O bio active glass form HCA crystalline layer on glass surface after 30 days of SBF soaking time for pelletized glass samples. HCA layer formation for sol–gel derived SiO_2–CaO–P_2O_5–Na_2O bio-glass strongly influenced by precursors such as tri ethyl phosphate (TEP) or phosphoric acid (H_3PO_3) (Siqueira and Edgar 2013). Based on CaO quantity, lower P_2O_5 content and higher molar SiO_2 content sol–gel derived calcium phosphosilicate glasses exhibit good bioactivity. Higher CaO content leads to amorphous nature of glasses before SBF treatment (Kiran et al. 2017). Recent study shows that barium with low concentrations in the glasses acts as a muscle stimulant and is found in human teeth (Carta et al. 2007). Bone stimulating property can be improved by incorporation of bone stimulator ions into their chemical compositions. Moreover, there are limited studies on the role of CaO substitution on apatite layer formation of barium-doped phosphosilicate glasses (Sampath Kumar et al. 2015; Kokubo and Takadama 2006) and on the importance of higher BaO contents on HCA-forming ability for sol–gel derived soda lime phospho silicate glass system.

The present study is focussed on the sol–gel synthesis of [$58SiO_2$–$(32 - x)$ BaO–xCao–$6Na_2O$–$4P_2O_5$ bioactive ($x = 15$, 20, 25 and 30 mol%)] composition. Thermal, structural properties of synthesised glass samples were studied using TGA/DTA analysis and XRD techniques for the confirmation glass-ceramic nature of the material. The non-bridging oxygens (NBO) and bridging oxygens (BO) in the synthesised composition were identified by FTIR and Raman spectroscopic techniques and further corresponding NBO/BO ratios were found using Raman spectroscopic analysis. The effect of NBO/BO ratio on early apatite layer formation for synthesised bioactive system has been investigated.

Materials and methods

Synthesis of barium doped soda lime Phosphosilicate glasses

$58SiO_2$–$(32 - x)$ BaO–xCaO–$6Na_2O$–$4P_2O_5$ ($x = 15$, 20, 25 and 30 mol%) samples were synthesised by conventional sol–gel process and named as CPSNB1, CPSNB2, CPSNB3 and CPSNB4, respectively, as shown in Table 1. The selected precursors for preparation were tetraethylorthosilicate [$Si(OC_2H_5)_4$] ($\geq$ 99%), triethylphosphate (TEP) [$(C_2H_5O)_3PO$] ($\geq$ 99%), calcium nitrate tetra hydrate [$Ca(NO_3)_24H_2O$] (98%), sodium nitrate ($NaNO_3$) (99%), barium nitrate [$Ba(NO_3)_2$] ($\geq$ 98%). Required chemicals for synthesis were purchased from Merck company (Mumbai, India). H_2O and HNO_3 (69%) were taken as [(mol of H_2O)/(mol of TEOS + mol of TEP) = 10] and [(mol of HNO_3)/(mol of TEOS + mol of TEP) = 0.05], respectively. In order to synthesise the glass sample, TEOS was mixed with H_2O and HNO_3 and stirred for 1 h. At an interval of 1 h, TEP, calcium nitrate, sodium nitrate and barium nitrate were added subsequently and stirred well. The prepared sols were poured into Teflon beakers, sealed and kept inside hot air oven at 60 °C temperature for 3 days for ageing purpose. Subsequently the aged gels were dried at 130 °C for 4 h. The dried gels were ground, made into powders and heated at the rate of 5 °C/min up to 700 °C and stabilised at that temperature for 4 h to obtain glass samples in the powder form. After getting powder samples, pellets have been prepared using hydraulic press by applying 5 tons of pressure for 5 min (Kiran et al. 2017).

Table 1 Batch composition of $58SiO_2$–$(32 - x)BaO$–$xCaO$–$6Na_2O$–$4P_2O_5$ glasses

Glass sample	SiO_2 (mol%)	P_2O_5 (mol%)	Na_2O (mol%)	BaO (mol%)	CaO (mol%)
CPSNB1	58	4	6	17	15
CPSNB2	58	4	6	12	20
CPSNB3	58	4	6	7	25
CPSNB4	58	4	6	2	30

Characterisation of bio-active glasses before and after soaking in SBF solution

The quantitative analysis is based on the glass transition (T_g) and onset crystallisation (T_x) temperatures of gel samples. T_g and T_x were identified by TGA and DTA analysis using SII EXTRAR 6000, Japan with flow rate of 10 °C/min in the temperature range 27–1000 °C. The crystalline nature of the samples was observed by JOEL, JDX-8P X-ray diffractometer (Japan) with CuK_α radiation within the range of diffraction angles 20°–80°. SHIMADZU FTIR spectrometer (North America) and LABRAM-HR 800 Laser Raman spectrometer (Japan) were used for analysis of the assigned bands in glass samples. To study the HCA growth properties for the synthesised samples, SBF solution has been selected as physiological environment which has similar properties as those of human blood plasma. The SBF solution was prepared by dissolving reagent grade KH_2PO_4 (≥ 98%), $CaCl_2$ (≥ 98%), $NaHCO_3$ (99%), $MgCl_2{\cdot}6H_2O$ (98%), KCl (99%) and NaCl (99%) in the de-ionised water at pH 7.4 with tris-buffer (99.8%) while maintaining temperature at 37 °C (Table 2). The pH values of SBF solution were measured using pH meter (Eutech, pH 510, India) before and after soaking CPSNB samples. $PO_4^{3-}$and Ca^{2+} ion concentrations were measured using UV/Vis absorption spectrometer (HITACHI PM & E 101, Canada) and Flame Photometer (ELICO CL378, Germany). The surface morphology of samples was observed by JOEL-JSM-6380LA, Japan, scanning electron microscope (SEM) and elements on surface were identified by EDX analyser after gold sputtering with JFC 1600 auto fine counter (JOEL, Japan). The presence of HCA layer was confirmed using XRD, SEM/EDX, TEM/SAED (JOEL Company JEM 2100 model, Japan), FTIR and Raman spectroscopic techniques.

Results and discussion

TGA/DTA analysis

TGA/DTA curves were recorded to find the thermal behaviour of CPSNB glasses. Three weight losses were observed in TGA curves as shown in Fig. 1a–d. The first weight loss was at 108–123 °C related to the evaporation of organics. The second weight loss was at 497–535 °C related to the elimination of water caged in pores and third was at 598–627 °C related to the organic residues from precursors used for samples synthesis and to dehydration process (Table 3). The glass transition temperatures were observed using DTA curves. These results dictated that CaO incorporation increases all the three temperatures, namely (1) the nucleation temperature (T_g) at 294–340 °C (2) the onset stabilisation temperature (T_{x1}) at 400–428 °C and (3) the crystallisation temperature (T_{c1}) at 420–472 °C range. These three temperatures were known to be related to primary crystalline phase (Marczewska et al. 2017; Shelby 2005). Second, third, fourth and fifth crystalline temperatures were also observed for CPSNB1, CPSNB2, CPSNB3 and CPSNB4 samples as shown in Table 5 (Zhao et al. 2010). From these observations it was concluded that mixed alkaline earth oxide effect favours the crystalline nature of the glass samples.

XRD analysis

Figure 2a shows the XRD pattern of CPSNB samples. All samples show broad hump at 20°–30° with some sharp intense peaks, indicating that all CPSNB samples had glass-ceramic nature. Crystalline peak intensities decreased for CPSNB samples with increasing CaO content from 15 to 30 mol%. All glass samples were sintered at 700 °C. Sintering temperature was higher than the onset crystalline

Table 2 Ion concentration (mM) in SBF and in human blood plasma

Fluid/ions	Na^+	K^+	Mg^{2+}	Ca^{2+}	Cl^-	HCO^{3-}	HPO_4^{2-}	SO_4^{2-}
SBF	142.0	5.0	1.5	2.5	147.8	4.2	1.0	0.5
Human plasma	142.0	5.0	1.5	2.5	103.0	27.0	1.0	0.5

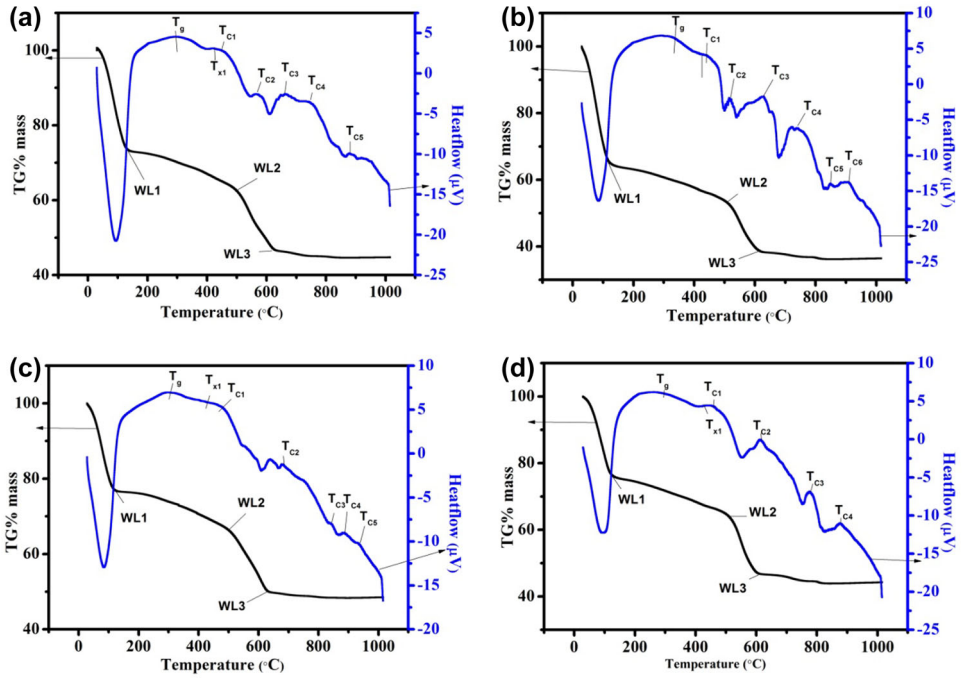

Fig. 1 TGA/DTA curves of **a** CPSNB1, **b** CPSNB2, **c** CPSNB3 and **d** CPSNB4 glasses

Table 3 TGA/DTA-related temperature values of $58SiO_2$–$(32 - x)BaO$–$xCaO$–$6Na_2O$–$4P_2O_5$ glasses

Glass	WL1 (%)	T_{WL1} (°C)	WL2 (%)	T_{WL2} (°C)	WL3 (%)	T_{WL3} (°C)	T_g (°C)	T_{X1} (°C)	T_{C1} (°C)	T_{C2} (°C)	T_{C3} (°C)	T_{C4} (°C)	T_{C5} (°C)
CPSNB1	73	113	64	528	46	603	294	400	420	581	649	767	881
CPSNB2	64	123	54	497	38	622	327	405	446	521	627	741	849
CPSNB3	76	108	67	511	50	627	333	425	456	753	884	888	934
CPSNB4	76	111	65	535	46	598	340	428	472	610	779	876	–

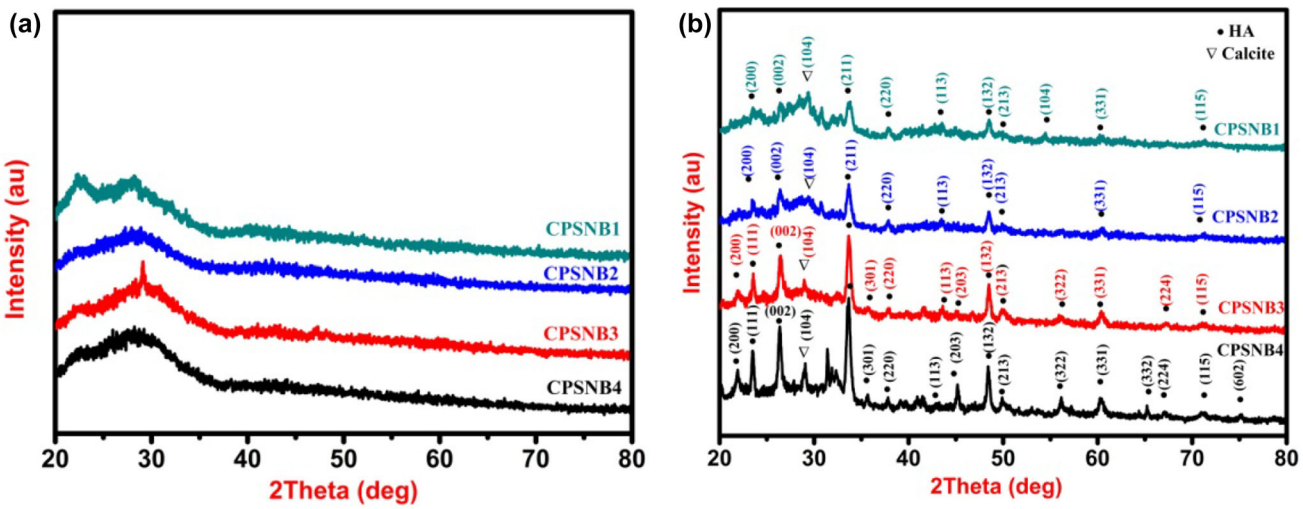

Fig. 2 XRD pattern of CPSNB samples **a** before and **b** after SBF treatment

temperature (As discussed in DTA curves). Due to this reason all glass samples showed crystalline peaks. The difference between sintering and onset crystalline temperatures was in decreasing order from CPSNB1 to CPSNB4 glass and leading to decrease in crystalline nature with CaO addition.

For SBF-treated CPSNB samples XRD pattern (Fig. 2b) showed HA crystalline peaks. The major diffraction peak was identified at $2\theta \sim 32°$ [(hkl) = (211)]. d-spacing of crystalline peaks were matched with the standard JCPDS file with number 01-074-0565. Calcite phase was also observed at 29° (JCPDF NO 01-081-2027). In SBF treatment, a chemical reaction occurs on sample surface. In this process Ca^{2+} ions migrate into SBF solution and form silanol (Si–OH) groups. Due to poly-condensation process silica gel layer forms on sample surface. Phosphate and calcium ions migrate through silica gel layer and form apatite layer on the sample surface. Due to crystallization process between apatite layer and prevalent hydroxyl, calcium, phosphate ions in SBF, HA layer form on sample surface. CPSNB1 sample has more BaO content than CPSNB2. BaO addition decreases the glass strength, increases the dissolution in SBF and it leads to increased HA formation on sample surface. For SBF-treated samples crystallite sizes were calculated for (211) and (132) planes using following Scherrer equation:

$$D = k\lambda/\beta\cos\theta,$$

where D is crystallite size, K is Scherrer constant, λ is wave length of CuK_α radiaton, β is full width half maximum (FWHM) and 2θ is the angle of diffraction. The measured FWHM and D values are as shown in Table 4. HA crystallite sizes were decreased with increasing CaO content from 15 to 20 mol%. It corroborates that HA-forming ability is more for CPSNB1 compared to CPSNB2 sample. HA crystallite sizes were increased from 20 to 30 mol % of CaO. HA layer formation depends on Ca^{2+} ions' dissolution in SBF solution. CaO quantity increases from CPSNB2 to CPSNB4 sample. Due to this reason Ca^{2+} ions' dissolution increases from CPSNB2 to CPSNB4 sample, which led to increase in HA crystalline intensity from CPSNB2 to CPSNB4 sample. It corroborates that HA-forming ability increases from CPSNB2 to CPSNB4 sample. From all these observations it was concluded that both the conditions, namely (i) higher BaO content and (ii) increase in CaO content favour the HA formation.

Surface morphology

Surface morphology of CPSNB samples before and after SBF treatment is shown in Figs. 3 and 4. Before SBF treatment (Fig. 3a–d) all CPSNB samples had not shown any spherical shaped crystalline particles and corresponding EDX analysis confirmed that elements present in sample were Ba, Si, Ca, Na, P and O. After SBF treatment the SEM images (Fig. 4a–d) clearly exhibited the spherical shaped nuclei on sample surface. As discussed in the previous section the crystallization process between apatite layer and existing hydroxyl, calcium, phosphate ions led to the formation of HA on sample surface. In this process, with the presence of CO_3^{2-}, HA gets converted into HCA. EDX analysis also supports the HCA layer formation on the CPSNB sample surfaces by identifying elements as Ca, P, C and O. EDX spectra show that Ca intensity decreased for CPSNB samples with increase in CaO content from 15 to 20 mol%. All SBF- treated CPSNB samples show good homogeneity in particle size and smooth spherical morphology with HCA particles (Fig. 5a–d). For CPSNB1 samples HCA average size is 1517 nm. For CPSNB2, CPSNB3 and CPSNB4 sample, average HCA particle sizes are 1355, 1587 and 1605 nm, respectively. This shows that average particle size decreases with increase in CaO content from 15 to 20 mol% and increases with increase in CaO content from 20 to 30 mol% (Yadav and Singh 2015). From these observations it could be concluded that HCA-forming ability is more for CPSNB1 compared to CPSNB2 sample and HA-forming ability is in increasing order from CPSNB2 to CPSNB4 sample as observed in XRD analysis.

Raman analysis

Figure 6a shows Raman spectra of CPSNB samples. For all CPSNB samples assigned D_2 modes were observed at the wave number range of 565–593 cm^{-1}. Si–O–NBO, Si–O–

Table 4 FWHM and crystallite size values of HA from XRD analysis for (211) and (132) planes

Sample name	(211) plane		(132) Plane	
	FWHM (β)	Crystallite size (D) (nm)	FWHM (β)	Crystallite size (D) (nm)
CPSNB1	0.4872	17.30	0.3106	28.03
CPSNB2	0.9961	8.33	0.4024	21.64
CPSNB3	0.5176	16.031	0.3462	25.15
CPSNB4	0.4535	18.30	0.3238	26.90

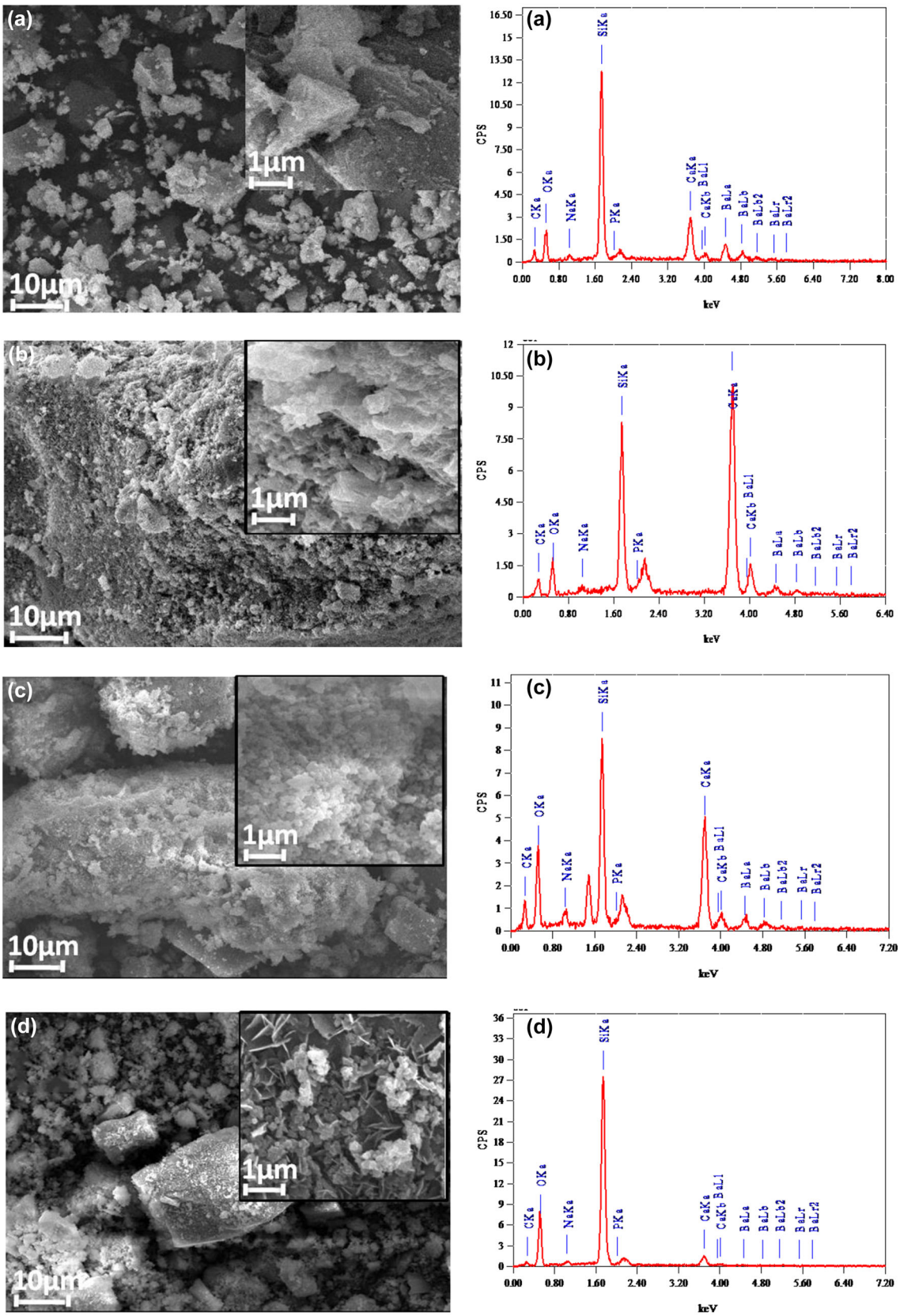

Fig. 3 SEM images of **a** CPSNB1, **b** CPSNB2, **c** CPSNB3 and **d** CPSNB4 glass samples and corresponding EDS spectra

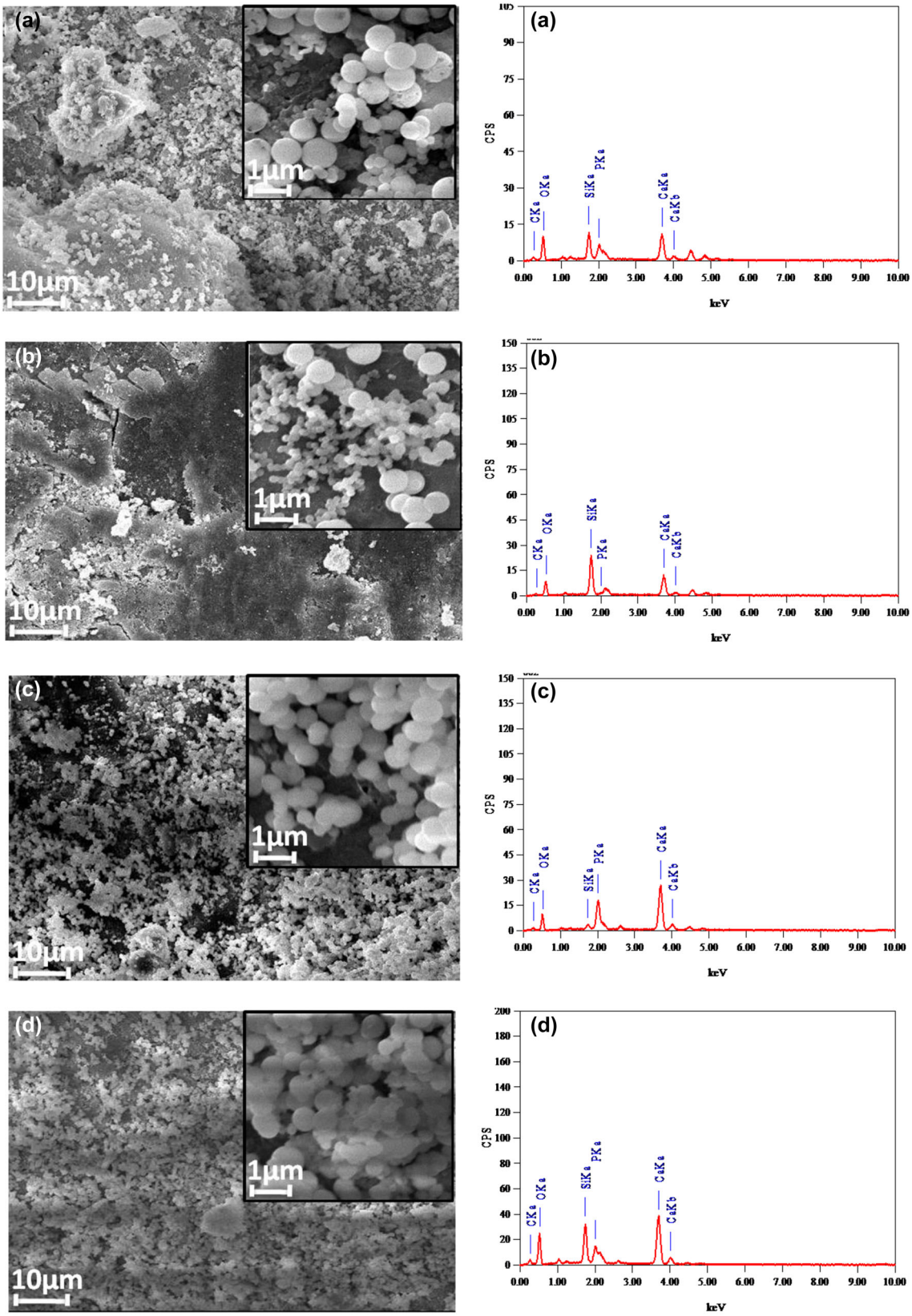

Fig. 4 SEM images of **a** CPSNB1, **b** CPSNB2, **c** CPSNB3 and **d** CPSNB4 glass samples after SBF treatment and corresponding EDS spectra

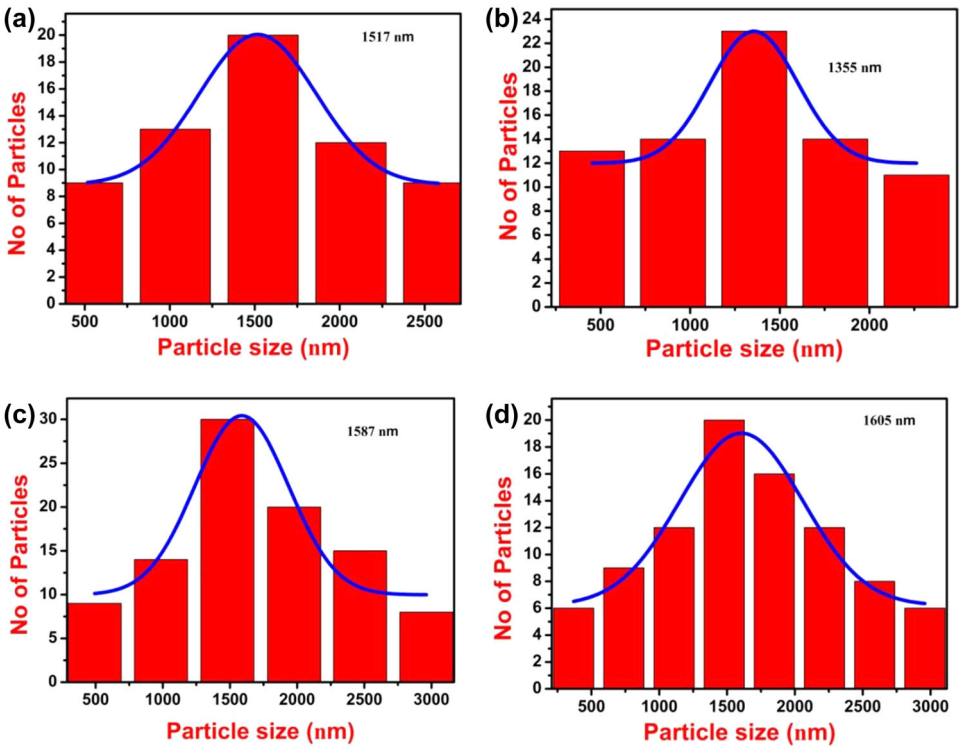

Fig. 5 HCA Particle size distributions for SBF soaked **a** CPSNB1, **b** CPSNB2, **c** CPSNB3 and **d** CPSNB4 glass samples

Si asymmetric stretching modes were observed at 956–965 and 1058–1068 cm^{-1}, respectively, as shown in Table 5. Using de-convolution process, non-bridging and bridging oxygen intensities were calculated (intensities were considered as corresponding fitted areas of Si–O–NBO, Si–O–Si asymmetric stretching modes) (Lucia et al. 2009). NBO/BO ratio varies with CaO as shown in Fig. 6b–e (Lucia et al. 2009). The obtained NBO/BO ratios for CPSNB1, CPSNB2, CPSNB3 and CPSNB4 samples were 0.36188, 0.22859, 0.26729 and 0.47349, respectively. It indicates that NBO/BO ratio decreased with increase in CaO from 15 to 20 mol% and increased with increase in CaO from 20 to 30 mol% (Yadav and Singh 2015). Wollstonite crystalline phase was also observed in the wave number region 1044–1051 cm^{-1} (Aguiar et al. 2009). For SBF-treated CPSNB samples, wollstanite crystalline phase has not been observed. It gave evidence to the fact that the wollstanite dissolved in SBF. Phosphate symmetric stretching, carbonate stretching vibrational modes were observed at 952–986 and 1076–1084 cm^{-1}, respectively, as shown in Fig. 6f (Table 6). CaO addition led to the deformation of Si–O–Si asymmetric stretching mode and formation of non-bridging oxygen modes (Fig. 7a). Si–O–Si stretching deformation causes not only Si–O–NBO formation, but also D_2 mode formation (Fig. 7b).

For SBF-treated CPSNB samples XRD pattern confirmed the HA formation. Raman spectroscopic analysis confirmed that carbonate groups were present. From these observations it was concluded that HCA layer formation was complete. SEM/EDX analysis also confirmed the HCA formation. Raman spectra confirmed that NBO/BO ratio decreased with CaO from 15 to 20 mol% and increased from 20 to 30 mol% (Fig. 7c). SEM/EDX analysis confirmed that HCA particle sizes decreased with CaO in the range 15–20 mol% and increased in the range from 20 to 30 mol%. From all these observations, it was concluded that NBO/BO ratio was proportional to HCA particle sizes of SBF treated CPSNB samples.

FTIR analysis

Figure 8a shows FTIR spectra of CPSNB samples in the wave number range 400–3500 cm^{-1}. Si–O–Si and Si–O–NBO asymmetric stretching modes related to silica matrix were observed at 1033–1103 and 925–948 cm^{-1}, respectively. Si–O–Si rocking, bending modes were observed at 478–486, 771–779 cm^{-1}, respectively. PO_4^{3-} and CO_3^{2-} bending modes were also observed at 594–624 and 1427 cm^{-1}, respectively. The vibration mode due to deformation of –OH groups was assigned at 1650–1658 cm^{-1} (Table 7).

For SBF-treated CPSNB samples (as shown in Table 8) Si–O–Si modes were related to Si–O–Si rocking, bending and asymmetric stretching modes are observed at 458–473, 729–786 and 1097–1243 cm^{-1}, respectively (Fig. 8b). Calcium group was observed as Si–O–Ca (as Si–O–NBO)

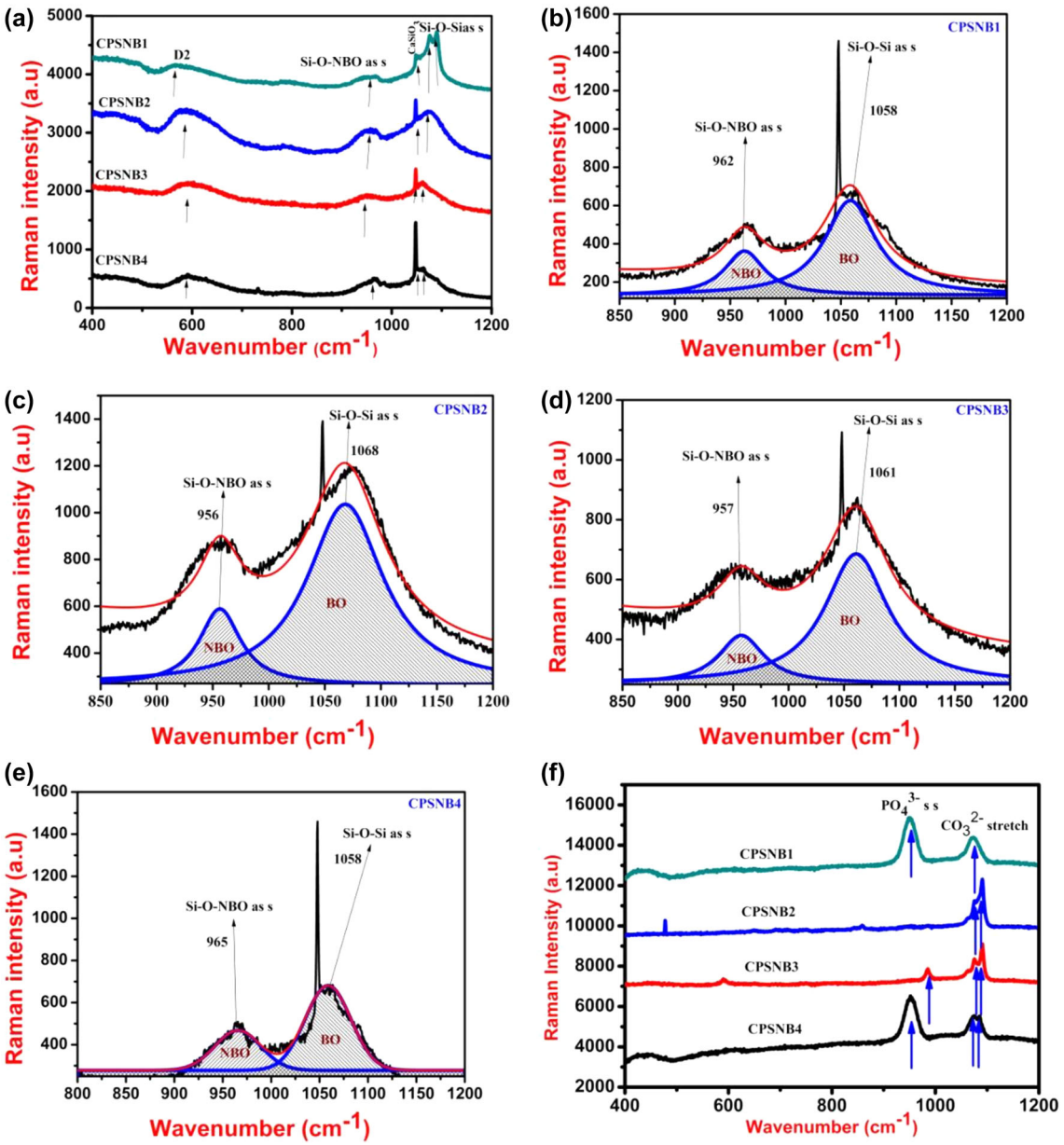

Fig. 6 **a** Raman spectra of $58SiO_2$–$(32 - x)$ BaO–xCaO–$6Na_2O$–$4P_2O_5$ system and the deconvoluted results of the, **b** sample CPSNB1, **c** sample CPSNB2, **d** sample CPSNB3, **e** sample CPSNB4 **f** Raman spectra of SBF treated $58SiO_2$–$(32 - x)$ BaO–xCaO–$6Na_2O$–$4P_2O_5$ system

Table 5 Raman absorption bands for $58SiO_2$–$(32 - x)$BaO–xCaO–$6Na_2O$–$4P_2O_5$ glasses before soaking in SBF solution

CPSNB1	CPSNB2	CPSNB3	CPSNB4	Assigned bands	References
Raman absorption band in cm^{-1}					
565	578	593	592	D_2	Notingher et al. (2003), Aguiar et al. (2008)
962	956	957	965	Si–O–NBO asymmetric stretching	Aguiar et al. (2009)
1058	1068	1061	1058	Si–O–Si asymmetric stretching	Aguiar et al. (2009)

at 879–928 cm^{-1}. CO_3^{2-} bending mode was also observed at 1471–1491 cm^{-1}. PO_4^{3-} bending modes with amorphous and crystalline nature were observed at 599–661 and 679–692 cm^{-1}, respectively. Si–O–Si asymmetric stretching mode broadness was increased for SBF-treated samples compared to synthesised samples, which shows that silica

Table 6 Raman absorption bands for $58SiO_2$–$(32 - x)BaO$–$xCaO$–$6Na_2O$–$4P_2O_5$ glasses after soaking in SBF solution for 7 days

CPSNB1	CPSNB2	CPSNB3	CPSNB4	Assigned bands	References
Raman absorption band in cm^{-1}					
958	952	986	952	PO_4^{3-} symmetric stretching	Aguiar et al. (2009), Rezwan et al. (2006)
1081	1084	1083	1076	CO_3^{2-} stretching	Aguiar et al. (2009), Rezwan et al. (2006), Notingher et al. (2003)

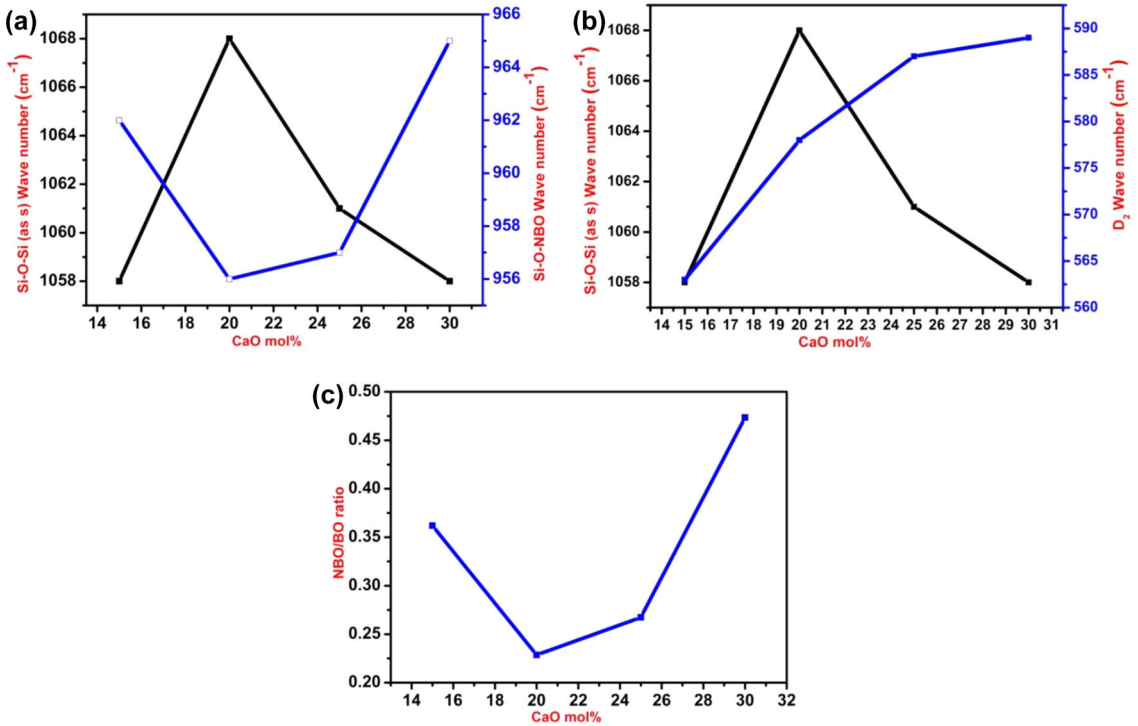

Fig. 7 **a** Variation of Raman shift of Si–O–NBO (as s) versus Si–O–Si (as s) with CaO mol%. **b** Variation of Raman shift of Si–O–Si (as s) versus D_2 with CaO mol%. **c** Variation of Raman Si–O–NBO (as s)/Si–O–Si (as s) intensity with CaO mol%

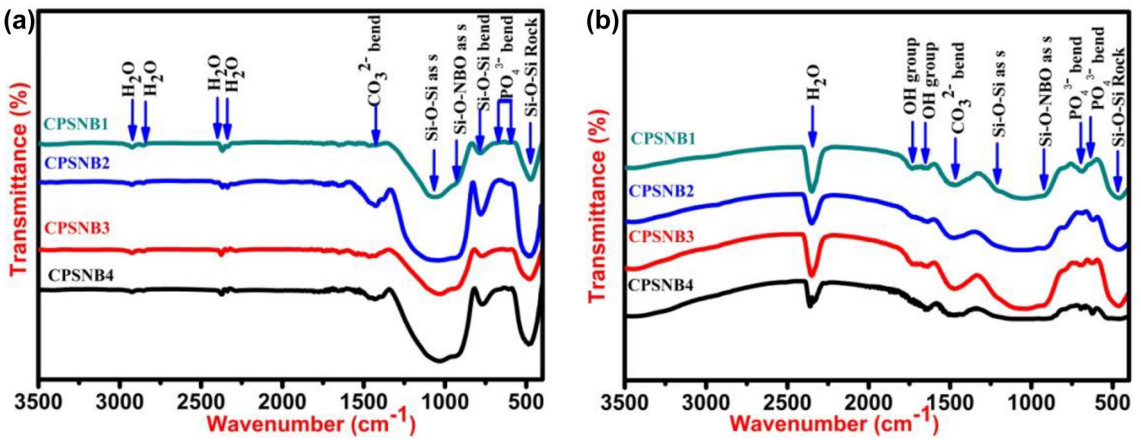

Fig. 8 FTIR spectra of CPSNB samples **a** before and **b** after SBF treatment

Table 7 FTIR band assignments of barium-doped soda lime phosphosilicate glasses before soaking in SBF solution

CPSNB1	CPSNB2	CPSNB3	CPSNB4	Assigned bands	References
486	486	478	478	Si–O–Si Rocking	Rezwan et al. (2006)
594	609	624	624	PO_4^{3-} bending	Rezwan et al. (2006)
779	771	771	771	Si–O–Si bending	Rezwan et al. (2006)
925	948	933	925	Si–O–NBO asymmetric stretching	Rezwan et al. (2006)
1087	1041	1033	1103	Si–O–Si asymmetric stretching	Rezwan et al. (2006)
1427	1427	1427	1427	C–O bending	Notingher et al. (2003)
1650	1658	1650	1650	–OH group	Notingher et al. (2003)

Infrared transition band in cm^{-1}

Table 8 FTIR band assignments of barium-doped soda lime phosphosilicate glasses after soaking in SBF solution for 7 days

CPSNB1	CPSNB2	CPSNB3	CPSNB4	Assigned bands	References
460	463	473	458	Si–O–Si rocking	Rezwan et al. (2006)
661	614	599	614	PO_4^{3-} bending amorphous	Kokubo and Takadama (2006)
687	692	679	687	PO_4^{3-} bending crystalline	Kokubo and Takadama (2006)
786	769	774	729	Si–O–Si (bending)	Rezwan et al. (2006)
928	879	909	920	Si–O–NBO (as s)	Rezwan et al. (2006)
1192	1185	1243	1097	Si–O–Si (as s)	Rezwan et al. (2006)
1472	1491	1489	1471	C–O bending	Aguiar et al. (2008)
1718	1637	1688	1699	–OH group	Kokubo and Takadama (2006)
2346	2363	2347	2337	H_2O molecule	Kokubo and Takadama (2006)

Infrared transition band in cm^{-1}

gel layer formed on the sample surface in poly condensation process. From these observations, it can be confirmed that HCA layer was completely formed in SBF treatment. OH groups and water molecules were observed at 1637–1718 and 2337–2363 cm^{-1}, respectively.

TEM/SAED analysis

Figure 9a, c, e and g reports the TEM images of SBF-treated CPSNB samples. Spherical shaped particles have been observed in TEM images. Using SAED pattern (Fig. 9b, d, f and h) d-spacing of relevant TEM images were calculated using the following formula:

$$d_{hkl} = \frac{\lambda L}{R},$$

where d_{hkl} = lattice spacing (nm), λ = wavelength of the TEM accelerating voltage (nm), L = camera length (mm), R = measured diffraction ring radius from a polycrystalline sample, or measured distance between two adjacent diffraction spots from a single crystal sample (mm) (John MC, Norrox Scientific Ltd, Ottawa, Canada, http://www.oocities.org/mag-i-cal@rogers.com/ABMcCaffrey-std-res.pdf).

The calculated d-spacings were matched with the d-spaces of HCA layer (Standard JCPDS card no.09-0432) (Table 9). Hence, it was concluded that the spherical shaped particles were HCA particles.

pH Assessment, dissolution and weight loss studies

In the dissolution process calcium ions get released into SBF solution, which led to silanol groups' (Si–OH) formation on sample surface. Due to the poly condensation process of silanol groups, silica gel layer was formed on sample surface. Ca^{2+} and PO_4^{3-} ions of sample leach on the silica gel layer surface, leading to calcium phosphate layer formation. This changes the phosphate and calcium ion concentrations of SBF solution. Incorporation of OH^-, PO_4^{3-}, Ca^{2+} and carbonate ions from SBF solution into apatite layer led to HCA formation on the sample surface (in the crystallization process). pH values of SBF solution were measured before and after soaking CPSNB samples in SBF for 7 days. As shown in Fig. 10a the pH values were

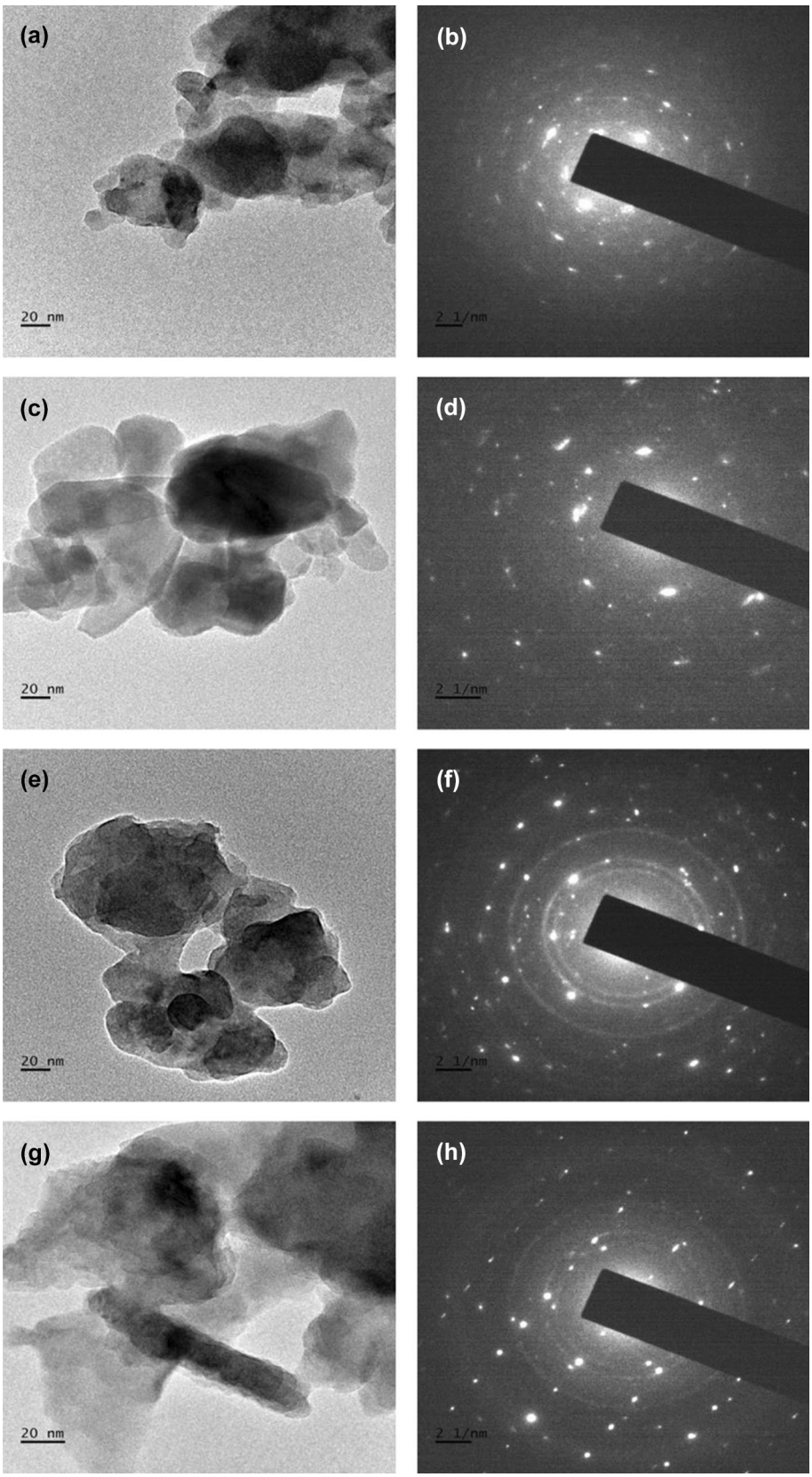

Fig. 9 TEM images of **a** CPSNB1, **c** CPSNB2, **e** CPSNB3 and **g** CPSNB4 glass samples and SAED pattern of **b** CPSNB1, **d** CPSNB2, **f** CPSNB3 and **h** CPSNB4 glass samples after SBF treatment

Table 9 Comparison of d-space for Hydroxyl apatite by SAED analysis and JCPDS file with Reference code: 01-086-0740

d_{hkl} (TEM)	CPSNB1 (nm)	CPSNB2 (nm)	CPSNB3 (nm)	CPSNB4 (nm)	d_{hkl} (JCPDS-01-086-0740)
$d_{(002)}$	0.3368	0.3349	0.3356	0.3372	0.3441
$d_{(202)}$	0.2649	0.2639	0.2651	0.2669	0.2622
$d_{(301)}$	0.2528	0.2498	0.2512	0.2531	0.2513
$d_{(213)}$	0.1817	0.1805	0.1811	0.1829	0.1835

increased till 10 h; this was due to the fast release of Ca^{2+} ions into SBF and forming silanol groups (Introduction to Glass Science et al. 2005). After 10 h pH values were almost stabilised.

For CPSNB1 sample, NBO/BO ratio is high compared to CPSNB2 sample. NBOs are in the form of Si–O–Ca. HA layer formation on sample surface depends on calcium, phosphate ions' dissolution of glass in SBF solution. NBO/BO ratio is also in the order CPSNB4 > CPSNB1 > CPSNB3 > CPSNB2. All CPSNB samples have 4 mol% P_2O_5. So, for SBF-treated samples CaO content plays major role for HA formation. Releasing Ca^{2+} ions into SBF for CPSNB samples are in the sample order of CPSNB4 > CPSNB1 > CPSNB3 > CPSNB2 and HA formation was also in the same (decreasing order) order Fig. 10b. From all these observations, it can be concluded that HCA formation is NBO/BO ratio dependent. Same observations were supported in XRD, SEM and EDX analyses also. Due to this, CPSNB samples' weight loss also changed (decreased) in the order of CPSNB4 > CPSNB1 > CPSNB3 > CPSNB2 (Table 10) (Fateme and Saeed 2013). Ba^{2+} ionic radius is more than Ca^{2+}. So, increase in BaO addition decreases the local field strength, leading to increase in dissolution of CPSNB sample. Compared to CPSNB2, CPSNB1 has more Ba^{2+} ions and leads to increase in Ca^{2+} and PO_4^{3-} ion dissolution in SBF. The number of Ba^{2+} ions is less, and the number of Ca^{2+} ions is more in CPSNB3 compared to

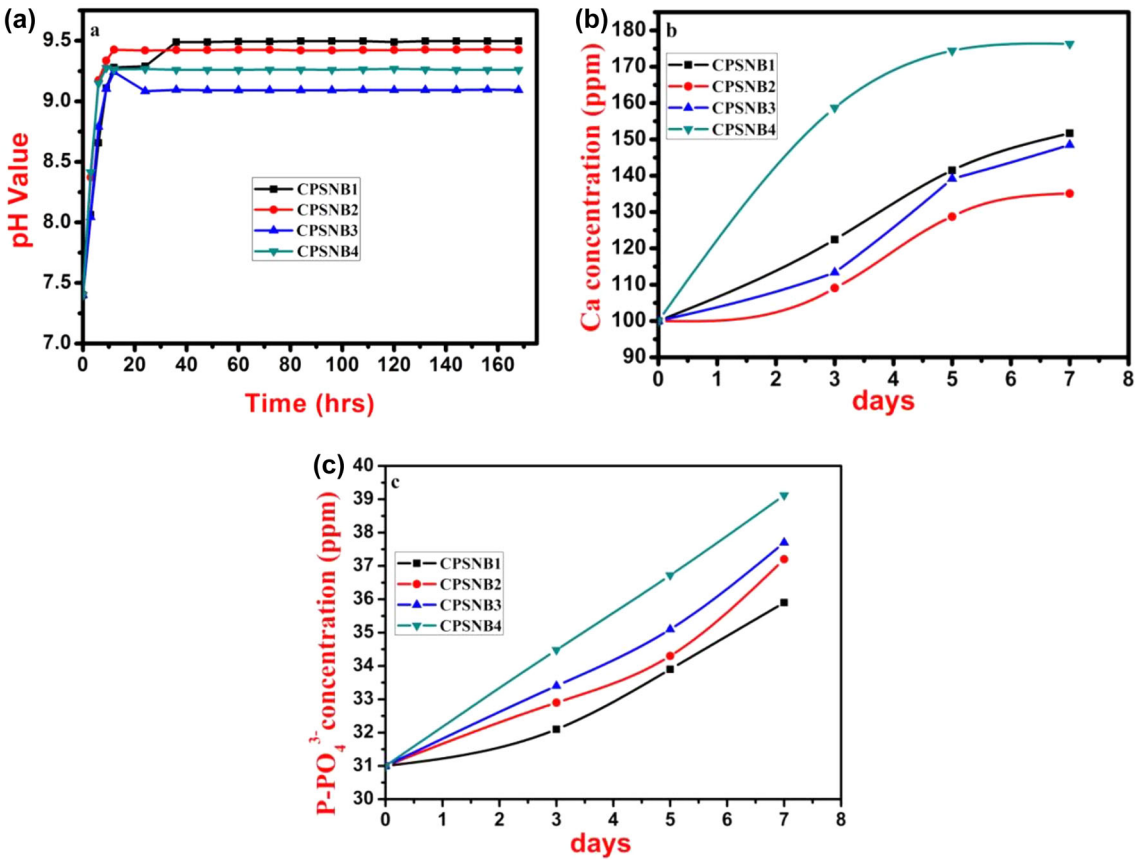

Fig. 10 Variation of **a** pH, **b** Ca concentration **c** P concentration values with respect to SBF soaking time for CPSNB glass samples

Table 10 Weight loss % of SBF soaked $58SiO_2$–$(32 - x)BaO$–$xCaO$–$6Na_2O$–$4P_2O_5$ glasses with NBO/BO ratio and HCA particle sizes

x mol%	(Raman) NBO/BO ratio	(SEM) Particle size (nm)	Weight loss for 7 days SBF soaking %
15	0.36188	1517	35.47
20	0.22859	1355	29.39
25	0.26729	1587	39.12
30	0.47349	1605	52.33

CPSNB2 sample, leading to increase in local field strength for CPSNB3 sample. Due to this reason PO_4^{3-} ions' release decreases in dissolution process for CPSNB3 compared to CPSNB2 sample. With low BaO, field strength is high for CPSNB4 compared to CPSNB3 sample. Due to this reason CPSNB4 sample releases less PO_4^{3-} ions into SBF solution compared to CPSNB3 sample. From these observations it could be concluded that decrease in BaO reduces the PO_4^{3-} dissolution. PO_4^{3-} ions' dissolution decreased from CPSNB1 to CPSNB4 sample. SBF solution needs to utilise PO_4^{3-} ions for HCA formation in the increasing order from CPSNB1 to CPSNB4 sample. So, phosphate ion concentration of SBF solution decreased for CPSNB1 to CPSNB4 sample as shown in Fig. 10c.

Conclusions

1. SiO_2–Na_2O–BaO–CaO–P_2O_5 glasses were synthesised using sol–gel method. DTA analysis confirmed that increase in CaO content increases the nucleation and crystallizationtemperature. XRD pattern confirmed that increase in CaO content increased amorphous nature of the synthesised glass.
2. NBO/BO ratio is proportional to HA crystallite size. For synthesised glasses NBO/BO ratio decreased with increase in CaO content from 15 to 20 mol% and increased with increase in CaO content from 20 to 30 mol%.
3. After 7 days of SBF treatment HCA particle sizes were decreased with increase in CaO content from 15 to 20 mol% and increased from 20 to 30 mol% of CaO which has been observed by EDX, XRD analysis, respectively. FTIR, Raman and TEM/SAED analysis confirmed that formed crystals are HCA crystals
4. Dissolution studies also confirmed that weight loss of samples decreased with increase in CaO from 15 to 20 mol% and increased with increasing CaO from 20 to 30 mol%. Weight loss of SBF-treated samples was proportional to NBO/BO ratio. From these observations it was concluded that both network modifiers (CaO and BaO) play their important roles in the formation of HCA layer in SBF treatment.
5. This work adds valuable information for the improvement of HCA growth rates for SBF-treated samples based on CaO and BaO quantities, in tissue engineering applications.

Acknowledgements The authors thank National Institute of Technology Karnataka, Surathkal, for providing research facilities and financial support. The authors thank to Prof. Trebbin (Hamburg Center for Ultrafast Imaging (CUI), University of Hamburg, Germany) for providing facilities.

References

Aguiar H, Solla EL, Serra J, Gonzalez P, Leon B, Almeida N, Cachinho S, Davim EJC, Correia R, Oliveira JM, Fernandes MHV (2008) Orthophosphate nanostructures in SiO_2–P_2O_5–CaO–Na_2O–MgO bioactive glasses. J Non-Cryst Solids 354:4075–4080

Aguiar H, Serra J, González P, León B (2009) Structural study of sol–gel silicate glasses by IR and Raman spectroscopies. J Non-Cryst Solids 355:475–480

Ahmed A, Simon CFR, Robert GH (2012) The role of MgO on thermal properties, structure and bioactivity of bioactive glass coating for dental implants. J Non-Cryst Solids 358:3019–3027

Arcos D, Vallet-Regíl M (2010) Sol–gel silica-based biomaterials and bone tissue regeneration. Acta Biomater 6:2874–2888

Bellucci D, Sola A, Salvatori R, Anesi A, Chiarini L, Cannillo V (2012) Sol–gel derived bioactive glasses with low tendency to crystallize: synthesis, post-sintering bioactivity and possible application for the production of porous scaffolds. Mater Sci Eng C 43:573–586

Bramhill J, Ross S, Ross G (2017) Bioactive nanocomposites for tissue repair and regeneration: a review. Public Health 14(1):66

Carta D, Knowles JC, Smith ME, Newport RJ (2007) Synthesis and structural characterization of P_2O_5–CaO–Na_2O sol–gel materials. J Non-Cryst Solids 353:1141–1149

Catauro M, Dell'Era A, Ciprioti SV (2016) Synthesis, structural, spectroscopic and thermoanalytical study of sol-gel derived

SiO_2−CaO–P_2O_5 gel and ceramic materials. Thermochim Acta 625:20–27
Fateme E, Saeed B (2013) Ali ABG. The effects of CaO/P_2O_5 molar ratio changes on in vitro bioactivity of nanopowder glass via sol–gel via sol-gel in SiO_2–CaO–P_2O_5 system. J Basic Appl Sci Res 3:375–382
Goldstein J (2003) Scanning electron microscopy and X-RAY microanalysis. ISBN 978-0-306-47292-3
Goller G, Oktar FN, Ozyegin LS, Kayali ES, Demirkesen E (2004) Plasma-sprayed human bone-derived hydroxyapatite coatings: effective and reliable. Mater Lett 58:2599–2604
Gonzalez P, Serra J, Liste S, Chiussi S, Leon B, Perez-Amor M (2003) Raman spectroscopic study of bioactive silica based glasses. J Non-Cryst Solids 320:92–99
Greenspan DC, Zhong JP, La Torre OH, Yli-Upro A (1994) Effect of surface area to volume ratio on in vitro surface reactions of bioactive glass particulates. Bioceramics 7:28–33
Greenspan DC, Zhong JP, Chen ZF, La Torre GP (1997) The evaluation of degradability of melt and sol–gel derived Bio-glass® in vitro. Bioceramics 10:391–394
Greenspan DC, Zhong JP, Wkeeler DL (1998) Bioactivity and biodegradability: melt vs. sol–gel derived bioglass in vitro and in vivo. Bioceramics 111:391–394
Hashmi MU, Shah SA, Umer F, Alkedy AS (2014) Effect of sintering temperature on microstructure and in vitro behavior of bioactive glass-ceramics. Ceram Silik 57:313–318
Hench LL, Polak JM (2002) Third-generation biomedical materials. Science 295:1014–1017
Hench LL, Splinter RJ, Allen WC, Greenlee TK (1971) Bonding mechanisms at the interface of ceramic prosthetic materials. J Biomed Mater Res Symp 334:117–141
John MC, Norrox Scientific Ltd, Ottawa, Canada, http://www.oocities.org/mag-i-cal@rogers.com/ABMcCaffrey-std-res.pdf
Kavitha RJ, Subha B, Shanmugam S, Ravichandran K (2014) Synthesis and invitro characterisation of lithium doped bioactive glass through quick alkali Sol-Gel method. Int J Innov Res Sci Eng 1(2):2347–3207
Kiran P, Ramakrishna V, Trebbin M, Udayashankar NK, Shashikala HD (2017) Effective role of CaO/P_2O_5 ratio on SiO_2–CaO–P_2O_5 glass system. J Adv Res 3:279–288
Kokubo T, Takadama H (2006a) How useful is SBF in predicting in vivo bone bioactivity? Biomater 27:2907–2915
Kokubo T, Takadama T (2006b) How useful is SBF in predicting in vivo bone bioactivity? Biomaterials 27:2907–2915
Kokubo T, Khushitani H, Sakka S, Kitsugi T, Yamamuro T (1990) Solutions able to reproduce in vivo surface-structure changes in bioactive glass-ceramic A-W[3]. J Biomed Mater Res 24:721
Laczka M, Cholewa-Kowalska K, Kulgawczyk K, Klisch K, Mozgawa W (1999) Structural examinations of gel-derived materials of the CaO–P_2O_5–SiO_2 system. J Mol Struct 511:223–231
Lucia M, Loredana M, Valter S, Chiara S (2009) Raman spectroscopic study of bioactive silica-based glasses: the role of the alkali/alkali earth ratio on the non-bridging oxygen/bridging oxygen (NBO/BO) ratio. Spectroscopy 23:227–232
Lukito D, Xue M, Wang J (2005) In vitro bioactivity assessment of 70 (wt.)% SiO_2–30 (wt.)% CaO bioactive glasses in simulated body fluid. Mater Lett 59:3267–3271
Lusvardi G, Malavasi G, Menabue L, Aina V, Morterra C (2009) Fluoride-containing bioactive glasses: surface reactivity in simulated body fluids solutions. Acta Biomater 5(9):3548–3562
Ma J, Chen CZ, Wang DG, Meng XG (2010) Influence of the sintering temperature on the structural feature and bioactivity of sol–gel derived SiO_2–CaO–P_2O_5 bioglass. Ceram Int 36:1911–1916
Marczewska A, Środa M, Nocuń M (2017) Thermal and spectroscopic characterization of gallium-tellurite glassesdoped BaF_2 and PbO. J Non-Cryst Solids 464:104–114
Notingher I, Boccaccini AR, Jones J, Maquet V, Hench LL (2003) Application of Raman microspectroscopy to the characterisation of bioactive materials. Mater Charact 49:255–260
Peitl O, Dutra Zanotto E, Hench LL (2001) Highly bioactive P_2O_5–Na_2O–CaO–SiO_2 glass-ceramics. J Non-Cryst Solids 292:115–126
Rezwan K, Qz Chen, Blaker JJ, Boccaccini AR (2006) Biodegradable and bioactive porous polymer/inorganic composite scaffolds for bone tissue engineering. Biomaterials 27:3413–3431
Rogar B, Antonio CS, Juliana M (2017) Evaluation of the bioactivity behavior of a 48 wt% SiO_2 bioglass through experiments in simulated body fluid. Mater Sci Forum 727–728:1238–1242
Sampath Kumar A, Himanshu T, Vikashkumar V, Shubham J, Shyamkumar S, Ram pyare SPS (2015) Influence of barium substitution on bioactivity, thermal and physico-mechanical properties of bioactive glass. Mat sci eng c 49:549–559
Shelby JE (2005) Introduction to glass science and technology, 2nd edn. The Royal Society of Chemistry, New York
Siqueira RL, Edgar DZ (2013) The influence of phosphorus precursors on the synthesis and bioactivity of SiO_2–CaO–P_2O_5 sol–gel glasses and glass–ceramics. J Mater Sci Mater Med 24:365–379
Sooksaen P, Pengsuwan N, Karawatthanaworrakul S, Pianpraditkul S (2015) Formation of porous apatite layer during in vitro study of hydroxyapatite-aw based glass composites. Adv Condens Matter Phys. doi:10.1155/2015/158582
Sooraj Hussain N, Lopes MA, Santos JD (2004) A comparative study of CaO–P2O5–SiO2 gels prepared by a sol–gel method. Mater Chem Phys 88:5–8
Sopcak T, Medvecky L, Girman V, Durisin J (2015) Mechanism of precipitation and phase composition of CaO–SiO_2–P_2O_5 systems synthesized by sol–gel method. J Non-Cryst Solids 415:16–23
Yadav AK, Singh P (2015) A review of the structures of oxide glasses by Raman spectroscopy. RSC Adv 5:67583
Yousef AM, Oudadesse H, Akbarzadeh R, Wers E, Lucas-Girot A (2014) Physical and biological characteristics of nanohydroxyapatite and bioactive glasses used for bone tissue engineering. Nanotechnol Rev 3:527–552
Zhao S, Li Y, Li D (2010) Synthesis and in vitro bioactivity of CaO–SiO_2–P_2O_5 mesoporous microspheres. Microporous Mesoporous Mater 135:67–73

Publisher's Note